

Journal of Materials Chemistry B

Accepted Manuscript



This article can be cited before page numbers have been issued, to do this please use: C. Bordeianu, A. Parat, C. Affolter-Zbaraszczuk, R. N. Muller, S. Boutry, S. Begin-Colin, F. Meyer, S. Laurent and D. Felder-Flesch, *J. Mater. Chem. B*, 2017, DOI: 10.1039/C7TB00781G.



This is an Accepted Manuscript, which has been through the Royal Society of Chemistry peer review process and has been accepted for publication.

Accepted Manuscripts are published online shortly after acceptance, before technical editing, formatting and proof reading. Using this free service, authors can make their results available to the community, in citable form, before we publish the edited article. We will replace this Accepted Manuscript with the edited and formatted Advance Article as soon as it is available.

You can find more information about Accepted Manuscripts in the [author guidelines](#).

Please note that technical editing may introduce minor changes to the text and/or graphics, which may alter content. The journal's standard [Terms & Conditions](#) and the ethical guidelines, outlined in our [author and reviewer resource centre](#), still apply. In no event shall the Royal Society of Chemistry be held responsible for any errors or omissions in this Accepted Manuscript or any consequences arising from the use of any information it contains.

ARTICLE

How a grafting anchor tailors cellular uptake and *in vivo* fate of dendronized iron oxide nanoparticles

Received 00th January 20xx,
Accepted 00th January 20xx

C. Bordeianu,^{a,b} A. Parat,^{a,b} C. Affolter-Zbaraszcuk,^c R. N. Muller,^{d,e} S. Boutry,^{d,e} S. Begin-Colin,^{a,b} F. Meyer,^{c*} S. Laurent^{d,e*} and D. Felder-Flesch^{a,b*}

DOI: 10.1039/x0xx00000x

www.rsc.org/

Superparamagnetic spherical iron oxide nanoparticles of 10 nm diameter have been synthesized by thermal decomposition and grafted through a direct ligand exchange protocol with two dendrons bearing respectively a monophosphonic anchor (D2) or a biphosphonic tweezer (D2-2P) at their focal point. Physico-chemical characterizations such as Dynamic Light Scattering (DLS), zeta potential, Fourier-Transform Infrared Spectroscopy (FTIR), Transmission Electron Microscopy (TEM) and Superconducting Quantum Interference Device (SQUID) assessed their composition, colloidal stability and magnetic properties. High-resolution Magic Angle Spinning (HR-MAS) Nuclear Magnetic Resonance (NMR) spectroscopy studies have been conducted to understand the organic shell composition and to determine both the grafting rate of the dendrons to the nanoparticles surface and the influence of the remaining oleic acid originating from the synthesis protocol on the cellular uptake. Both dendronized IONPs showed moderate *in vitro* toxicity (MTT and LDH tests) on human cancer and primary cell lines. Furthermore, *in vivo* MRI studies showed high contrast enhancement as well as renal and hepato-biliary excretions and highlighted the influence of the grafting anchor (mono- versus bi-phosphonate) toward the *in vivo* fate of dendronized magnetic iron oxides.

Introduction

Although progress in the application of nanotechnology has been dramatic and successful,¹ substantial opportunities exist for the development of future generation nanotherapeutics by improving upon certain recognized nanoparticle limitations such as instability, non-specific uptake and liver sequestration often due to *in vivo* aggregation.² Understanding the influence of nanoparticle properties – critical nanoscale design parameter (CNDPs) – on clinical translation issues, such as pharmacokinetics (PKs), pharmacodynamics (PDs), bioaccumulation, excretion modes and toxicology, is of utmost importance. These CNDPs include size, shape, surface chemistry, flexibility/rigidity, architecture and elemental composition. The ability to structure, control and engineer CNDPs is undoubtedly the major challenge in the translation of

nanoparticle-based therapeutics into approved clinical applications.³⁻⁴

Nano-objects offer several advantages to address unmet challenges in medicine: i) with tailored dimensions in the range of 10-100 nm, they are small enough to circulate in every capillary vessel of the organism allowing a non-invasive approach, ii) with their modular design and broad spectrum of functionalization, they have potential to simultaneously deliver drug and allow imaging,⁵ to achieve specific cell-targeting while maintaining stability in the blood⁶ which remains challenging with other molecular, remote or surgical approaches. Additionally with the aim to collect real-time data during a cancer treatment and understand how the nanovectors interact with a patient, the development of nanovectors allowing imaging is also crucial for the development of image-guided therapy.⁷

Among currently developed nano-objects, iron oxide NPs, due to their intrinsic properties, are extensively studied for different applications in the biomedical field.⁸ They are used for diagnosis as contrast agent for MRI,⁹ or as biosensors.¹⁰ In therapy, magnetic NPs are used as heating medium for hyperthermia treatment¹¹ or as a platform for drug delivery.¹² Iron oxide NPs are also used for purification and cell isolation.¹³ Depending on the synthesis method, iron oxide NPs may be both naked and dispersed in water (co-precipitation technique), or *in situ* coated with surfactants and dispersed in an organic solvent (thermal decomposition).¹⁴ Different grafting strategies have been developed according to the nature of the molecule,

^a Université de Strasbourg, CNRS, Institut de Physique et Chimie des Matériaux de Strasbourg, UMR 7504, F-67000 Strasbourg, France. *Email - Delphine.Felder@ipcms.unistra.fr

^b Fondation IcFRC/Université de Strasbourg, 8 allée Gaspard Monge BP 70028 F - 67083 Strasbourg Cedex.

^c Université de Strasbourg, INSERM, UMR 1121 Biomatériaux et Bioingénierie, 11 rue Humann 67000 Strasbourg, France *Email - fmeyer@unistra.fr

^d University of Mons, General, Organic and Biomedical Chemistry NMR and Molecular Imaging Laboratory, Avenue Maistriau 19, 7000 Mons, Belgium

^e CMMI - Center for Microscopy and Molecular Imaging, MRI & Optical Imaging, Rue Adrienne Bolland 8, 6041 Gosselies, Belgium

Electronic Supplementary Information (ESI) available: [Synthesis and characterization of the Dendron D2-2P; characterizations of the nanoparticles NP10@OA and *in vitro* supplementary data]. See DOI: 10.1039/x0xx00000x

the NPs synthetic methods or surface, and the solvents.¹⁵ Two major approaches depending on the NPs synthetic method are reported to functionalize the NPs: in situ coating (when the nucleation of the magnetic cores occurs within the coating materials, "one-pot" synthesis)¹⁶ or post synthetic coating. The post synthetic coating process is often used and relies on coating materials that are connected to the magnetic cores surface mainly through direct grafting, ligand exchange, or hydrophobic interactions.¹⁷ Direct grafting is developed by introducing molecules in water or organic NPs suspensions. NPs coating through ligand exchange or hydrophobic interactions is mainly performed with NPs coated in situ by surfactants such as oleic acid (OA). One must then know that unsaturated fatty acids such as OA, in conjunction with cytotoxicity, are internalized, within minutes, by receptor-mediate mechanisms or by diffusion across the cell membranes.¹⁸ This has been attributed to the higher disrupting nature of the kinked chain of these fatty acids that would result in higher magnitude of lipid disruption¹⁹ thus leading to increased cellular uptake.

In the case of biomedical applications, the functionalization of NPs is of major importance and must meet a set of specific characteristics such as i) bring biocompatibility and hydrophilicity, ii) ensure stealth NPs, iii) allow the colloidal stability of NPs in water, in physiological media rich in proteins and in the presence of high electrolyte concentration without desorption of molecules, iv) conduct to a mean hydrodynamic size less than 100 nm after functionalization to ensure a good biodistribution, and v) provide functional groups for coupling of bioactive molecules. The nature of the surface functionalization of the NPs and the grafting method will condition these parameters. The hydrodynamic diameter of the NPs after functionalization is an important parameter, especially if intravenous injection is envisioned. Thus, it is more favorable to graft small molecules to the NPs's surface that will cover uniformly the surface while minimizing their final size: this is not always possible when polymers are grafted on NPs. Considering this issue, the grafting of dendron (elementary unit of a dendrimer) appears as a good approach for the functionalization of NPs for biomedical applications.²⁰ Indeed, their small size ensures a final low hydrodynamic diameter, their tree structure provides high stability in suspension and their various functional groups allow providing additional multifunctionality to the final nano-object. Regarding stability, M. Textor et al. have compared iron oxide nanoparticles (IONPs) colloidal suspensions functionalized with linear or dendritic PEG chains of various molecular weights.²¹ They demonstrated the reversible aggregation of NPs functionalized with dendrons at increased temperature, while NPs functionalized with linear molecules aggregate and sediment irreversibly. The group of Na et al.²² has, in the meanwhile, compared two branched versus two linear structures, bearing carboxylic acids or catechol as coupling agents: the branched structure increases the colloidal stability in water, in a 1M NaCl solution, and in a medium used for cell culture. Recently, Walter et al.²³ functionalized iron oxide NPs of 10 nm with a linear PEG monophosphonate or with PEGylated mono-phosphonated dendrons of growing generations: dendritic nano-objects with a mean hydrodynamic

size smaller than 50 nm, stable in physiological media and showing both renal and hepatobiliary elimination have been obtained. The colloidal stability is induced by combined electrostatic and steric interactions when only electrostatic interactions are involved in the colloidal stability of hybrids grafted with a linear molecule. These last nano-objects were less stable in biological media at high ionic concentration and Nuclear Magnetic Resonance Dynamic (NMRD) profiles and relaxivity measurements highlighted the influence of the molecule architecture on the water diffusion close to the magnetic core thus influencing the relaxation properties at low magnetic field.

The influence of the dendron generation was the subject of several articles: the increase in generation also increases the functionality of the NPs. In 2012, the team of K. Kono showed that transfection activity of PAMAM dendron bearing lipids depends on the dendron generation.²⁴ Duanmu et al.²⁵ have particularly shown the influence of the dendron generation on the MRI properties of iron oxide NPs: the r_2 relaxivity increased with dendron generation. Walter et al.²³ confirmed this result and showed that the dendron architecture was also an important parameter.

In this paper we report on the synthesis of spherical 10nm IONPs by thermal decomposition in the presence of surface active agents (OA) acting as stabilizers and offering a good colloidal stability in non-polar organic solvents. IONPs hydrophilicity and suitability for biomedical applications is provided by their functionalization with two types of dendrons, D2 and D2-2P (Fig. 1), fully oligoethyleneglycol dendrons displaying either one (D2) or two (D2-2P) phosphonic acids at their focal point and a long functional octaethyleneglycol chain in para position bearing a carboxylate end-group. The resulting dendronized IONPs have been characterized, their physico-chemical properties discussed. We show that their toxicity, in vitro and in vivo fate is highly dependent on the anchoring group (mono-phosphonic acid (D2) or phosphonic tweezer (D2-2P)) and subsequently on the remaining amount of OA at the surface of dendronized NPs.

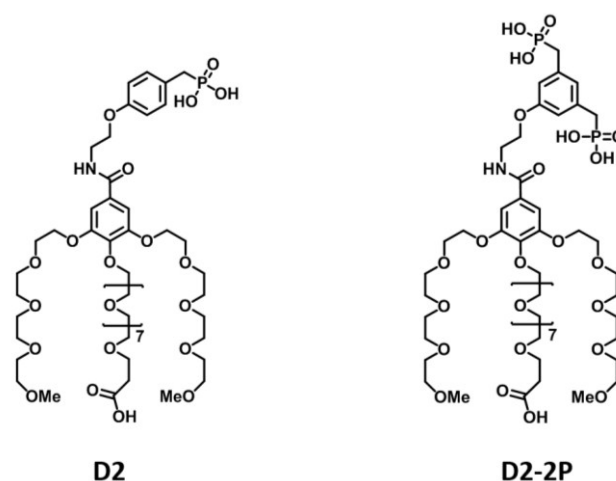


Figure 1. Dendritic phosphonic acids grafted on the surface of spherical iron oxide nanoparticles.

Results and discussion

The FTIR profiles of NPs10@OA washed 3 and 6 times are represented in ESI (Fig. S1) and display three distinct zones: the bands between 3000 and 2800 cm⁻¹ which are attributed to alkyl chains of OA, those between 1800 and 900 cm⁻¹ to the asymmetric and symmetric COO⁻ bands of oleate and those between 800 and 500 cm⁻¹ to Fe–O bands of iron oxide.

The narrow band between 1800 and 1700 cm⁻¹ corresponds to the vibration of COO⁻ double bond of free OA molecules in the suspension of NPs10. Furthermore, the bands located at 1660 and 1390 cm⁻¹ are characteristic of asymmetric and symmetric vibrations of OA grafted to IONPs surface via carboxylate function. The band at 719 cm⁻¹ is characteristic of the presence of iron stearate and IONPs magnetite phase displays one Fe–O characteristic band at around 570 cm⁻¹.

The purification efficiency of IONPs by centrifugation was determined evaluating the intensity ratios between bonded and free OA, and between Fe–O bond relative to iron stearate and NPs10. The intensity ratio of C–H and Fe–O bonds decreases with the number of washes, indicating elimination of residual organic molecules (Stearate and OA). Similarly, the peaks corresponding to COO⁻ bond of free OA and Fe–O of iron stearate decrease with the number of washes. NPs10 are considered as “washed” when Iron stearate band disappears and the band intensity of the C=O double bond is low. Purification process is tricky due to the equilibrium between bonded and free OA in the solution. If NPs10 are too “washed”, OA tend to maintain the equilibrium and desorb from IONPs surface, leading to aggregation. Following the previous purification process, it results to an optimal amount of OA on the surface of NPs, which is very important for further functionalization with dendrons.

The size distribution of NPs10 stabilized with OA (NPs10@OA) has been determined by TEM and DLS analysis (ESI, Fig. S2). NPs10@OA demonstrate a spherical morphology with an average size of 10 nm with a narrow size distribution (< 9%) and a polydispersity index (PDI) equal to 0.98. On the high resolution TEM image (ESI, Fig. S2) crystallographic planes are continuous for overall nanoparticles, showing a single crystalline domain in accordance with our previously published results.²⁶ NPs10@OA hydrodynamic diameter was evaluated by DLS measurements and compared to TEM size distribution (ESI, Fig. S2). DLS data show a monomodal size distribution with an average hydrodynamic diameter of 12 nm and a PDI = 0.043 in agreement with NPs shelled with oleic acid. TEM and DLS size distributions are unimodal, indicating a monodisperse colloidal system.

NPs10@OA magnetic and relaxometric properties were further characterized by SQUID magnetometry and NMRD profiles.

Zero Field Cooled (ZFC) and Field Cooled (FC) curves of NPs10@OA are characteristic of *superparamagnetic* NPs (ESI, Fig. S3): the maximum of ZFC curve, usually assimilated as the blocking temperature (T_B) is at 98 K and indicates a transition from magnetically blocked state (low temperature) to a superparamagnetic state (at high temperatures). Above the *superparamagnetic* transition temperature, T_B , particles behave as *paramagnets* due to the dominance of the thermal

fluctuations over the magneto-crystalline anisotropy energy. At low temperatures, below $T_B = 98$ K, the orientations of the particle's magnetic moments are frozen (so called blocked) in random directions and cannot rotate freely. Therefore, the sample magnetization becomes very small. Moreover, narrow ZFC curve reflects the fact that NPs10@OA sample has a very thin size distribution (10.6 ± 0.98 nm). Therefore the magnetization curve of NPs10@OA measured at 5 K presents a loop representative as expected, of a ferrimagnetic behavior (ESI, Fig. S3). The saturation magnetization M_s is of 60 ± 5 A.m².Kg⁻¹ and in agreement with published M_s value for NPs with similar size.¹⁷ The value of saturation magnetization of iron oxide NPs is generally lower than those of bulk magnetite and maghemite and is related to the composition evolution (from magnetite to maghemite) and to the presence of oxidation defects, surface spin canting and volume spin canting as a function of NPs diameter.¹⁷

Nuclear Magnetic Resonance Dynamic (NMRD) profile has been measured with Stellar fast field cycling NMR relaxometer at 37°C and displays the evolution of proton longitudinal relaxivity as a function of the applied magnetic field. NMRD profile recorded for NPs10@OA in THF is represented in ESI (Fig. S4).

According to the fitting of NMRD profile, one can extract theoretical values such as the saturation magnetization (M_s) and the relaxometric diameter (d^{NMRD}) which represents the shorter distance between magnetic core and THF molecules.

The general shape of the NMRD profile is similar and match very well to the NMRD curve of superparamagnetic colloidal suspensions.²⁷ The obtained NMRD diameter $d^{NMRD} = 10.9$ nm is slightly higher than TEM diameter. This observation is due to the thickness of OA, moreover, TEM calculations depend on the crystal volume.

Proton longitudinal relaxivity maximum is situated around 10 MHz, which fits the superparamagnetic model. M_s calculated from NMRD profile is close to 32 A.m².Kg⁻¹ of iron. The saturation magnetization estimated from NMRD profile can be considered as an approximated value. Indeed, the estimated magnetization is correlated to the distance of the solvent molecules surrounding the magnetic core. Else, OA at the NPs surface limits the approach of THF molecules near to the magnetic core, inducing inevitably an M_s decrease estimated by the fitting of the NMRD curve. Moreover, at high Larmor frequencies some differences can be observed on NMRD profile in comparison to the theoretical data. This can be explained by the influence of the solvent, as in THF all hydrogens are not equivalent and the heterogeneity of the proton signal increases with Larmor frequency. In theory, the evolution of relaxation time should be multi-exponential. However, in order to facilitate the measurements, a mono-exponential behavior was assumed. These assumptions can thus explain the small differences at high magnetic field. Table 1 summarizes diameter values obtained by various techniques (DLS, TEM and NMRD) and shows good correlation. Moreover, all of the values are coherent, since the theoretical order is followed $d^{DLS} > d^{NMRD} > d^{TEM}$. Fe³⁺ concentration values were measured with several techniques (Inductively Coupled Plasma (ICP), Atomic Absorption Spectroscopy (AAS) and Relaxometry).

Table 1. Summary of NPs10@OA sample size distribution and concentration values determined by different techniques.

	DLS	TEM	NMRD
Diameter (nm)	12 ± 0.043	10.6 ± 0.98	10.9 ± 1
	ICP-OES	AAS	Relaxometry
[Fe ³⁺] (mg/mL)	2 ± 0.02	2.2 ± 0.02	2.08 ± 0.06
[Fe ³⁺] (mM)	35.8 ± 1	39.4 ± 1	37.2 ± 3

Boutry *et al.* have established a robust relaxometric method for Fe³⁺ quantification in solutions, based on magnetic influence of iron ions on water protons relaxometry.²⁸ However, this technique can be applied to solutions containing only one type of magnetic ions, else there will be an impeding for one ion quantification.

Grafting and characterization

Nanoparticles NPs10@OA synthesized by thermal decomposition have a good colloidal stability in organic solvents. However, for biomedical applications surface ligands have to render IONPs hydrophilic, biocompatible and provide colloidal stability in water and physiological media. In this section, physico-chemical properties of IONPs functionalized with two dendrons, D2 and D2-2P, will be discussed and we will put into evidence their dependence on the anchoring group (mono- (D2) versus bi-phosphonic acid (D2-2P)).

Both stability and size distribution of dendronized NPs were determined by DLS and TEM measurements (Fig.2). After dendronization, size distributions of NPs10@D2 and D2-2P suspensions are monomodal with an average hydrodynamic diameter slightly larger than the one of NPs10@OA in THF (Fig.2 bottom). This slight increase is due to the larger length of the dendrons (2-3nm) by comparison with OA (from 1 to 2nm) (Table 2).

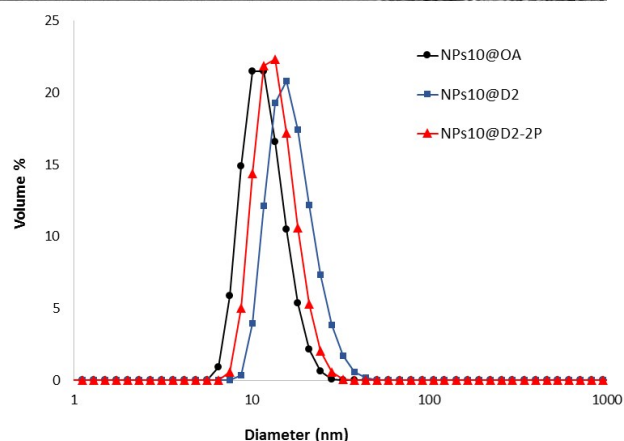
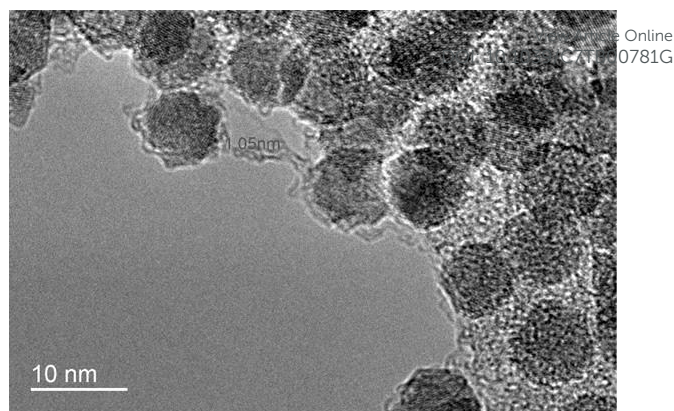


Figure 2. (Top) An example of dendronized NPs TEM image, NPs10@D2 and (down) size distribution by volume before (NPs10@OA) and after grafting with D2 and D2-2P (NPs10@D2 and NPs10@D2-2P).

Zeta potential measurements were done at physiological pH, around 7.4 (Table 2). The isoelectric point (IEP) for uncoated IONPs is equal to pH = 6.5 and thus naked IONPs are not stable in water suspension. The Zeta potential negative values obtained for dendronized NPs confirm the dendron grafting and are due to the presence of peripheral carboxylic acid functions (pKa=4), which are deprotonated at physiological pH. Colloidal stability is due to the electrostatic interactions introduced by the deprotonated carboxylate end groups and also to steric hindrance induced by the dendron architecture.²³

Table 2. Comparison between size distribution by volume of NPs10@D2 and NPs10@D2-2P determined by DLS, and corresponding Zeta potential values measured at pH = 7.4.

	d _{DLS} (nm)	PDI	Z potential (mV)	IEP
NPs10@OA	12 ± 1.3	0.043	-	-
NPs10@D2	17 ± 1.5	0.33	-16.9	2.9
NPs10@D2-2P	14 ± 1.1	0.29	-18.5	2.5

The surface modification of NPs10@OA with D2 and D2-2P has been assessed by FTIR spectroscopy (Fig. 3), comparing profiles of free dendrons with those of NPs before and after ligand exchange.

The FTIR profiles of NPs10 before and after functionalization with D2 and D2-2P display several bands characteristic of asymmetric and symmetric vibrations of CH_2 groups identified as $\nu_{\text{as}}(\text{C-H}) = 2920\text{cm}^{-1}$ and $\nu_{\text{s}}(\text{C-H}) = 2850\text{cm}^{-1}$.

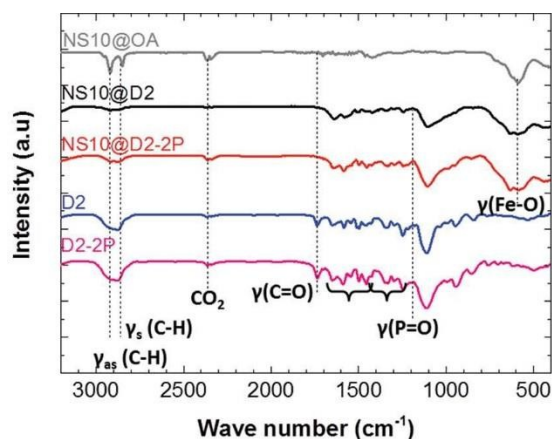


Figure 3. FTIR spectra of dendrons D2 and D2-2P and of NPs10 before and after functionalization with D2 and D2-2P.

The band at 1734cm^{-1} belongs to the carboxylic acid function. After the grafting of both D2 and D2-2P dendrons, the band belonging to the carboxylic acid function is not visible, which can be certainly attributed to the lower amount of carboxylate group carried by D2 and D2-2P (one COOH per 3 PEG chains). The C-O-C groups of PEG chains are characterized by bands at 1100cm^{-1} . This last band should also include the C-C-C groups of the aromatic cycle. The band at 1180cm^{-1} is attributed to the P=O double bond and bands at 1054 and 993cm^{-1} to P-OH bonds. IR spectrum of NPs10@OA displays a broad band for Fe-O located at 570cm^{-1} , whereas, dendronized NPs present small shoulders between 800 and 600cm^{-1} , attributed to a small surface oxidation.¹⁷

ZFC/FC curves of dendronized NPs (Fig. 4 right) are characteristic of superparamagnetic NPs. The maximum of the ZFC curve assimilated as the blocking temperature is $T_{\text{B}} = 68\text{K}$, smaller than that of NPs10@OA for which $T_{\text{B}} = 98\text{K}$. Indeed the blocking temperature is sensitive to the strength of dipolar interaction between magnetic NPs and the smaller T_{B} , the weaker the dipolar interaction strength. Thus the T_{B} value confirms the dendron coating which contributes to increasing the interparticle distances.

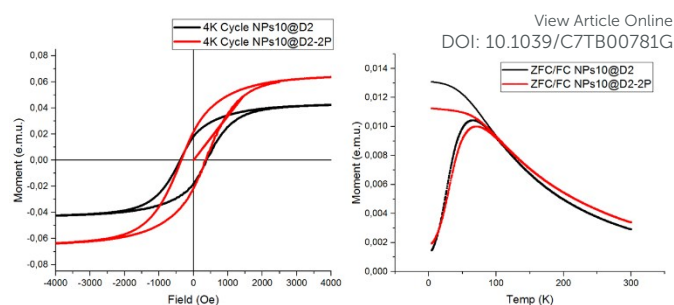


Figure 4. Hysteresis loop recorded at 4K (left) and temperature dependence of ZFC and FC magnetization (right) for NPs10@D2 and NPs10@D2-2P samples.

Magnetization curves of NPs10@D2 and D2-2P measured at 4K present, as expected, a loop, representative of a ferrimagnetic behavior (Fig. 4 left). M_{s} of 63 and $65\text{A.m}^2.\text{Kg}^{-1}$ were recorded for NPs10@D2 and NPs10@D2-2P, respectively, and are in agreement with the M_{s} value before grafting. Indeed the dendronization of NPs using phosphonate anchoring groups has already been demonstrated to preserve the magnetic properties of iron oxide NPs even if a small oxydation of $\text{Fe}_{3-x}\text{O}_4$ NPs occurred during the dendronization step.²⁶

According to the NMRD profiles (Fig. 5) the maximum longitudinal relaxivity peaks for dendronized and OA coated NPs are observed at the same positions, around 10MHz , since the size of all nanocrystals is similar. One must than notice that the NMRD profile of NPs10@OA has been recorded in THF, whereas it was recorded in water for both dendronized NPs10@D2 and NPs10@D2-2P, rendering the comparison of relaxivity values r_1 impossible between OA-coated or dendronized NPs.

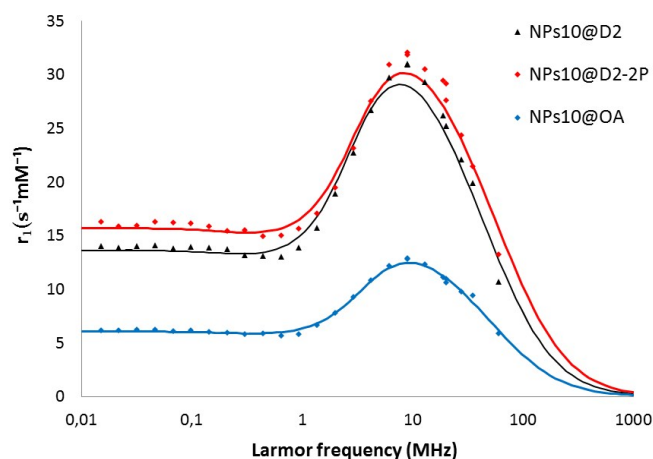


Figure 5. NMRD profiles of NPs10 before and after functionalization with both dendrons D2 and D2-2P.

Regarding only dendronized NPs10, the $r_{1\text{max}}$ value of NS10@D2 is slightly lower than the $r_{1\text{max}}$ value of NS10@D2-2P. The experimental data were fitted using the usual model assuming

a spherical shape of the particles. The M_s and diameter fitted values are shown in **Table 3**.

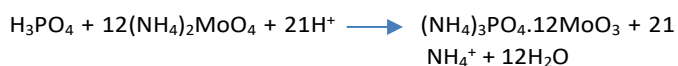
	NPs10@D2	NPs10@D2-2P
d_{NMRD} (nm)	10.6±1.6	10.1±1.7
r_1 (s-1.mM-1)	10.7±1	13.2±2
r_2 (s-1.mM-1)	74.5±3	70.7±5
r_2/r_1	6.9±0.5	5.3±0.3
M_s^{NMRD} (A.m ² .kg ⁻¹)	46±0.2	53±0.3
M_s^{SQUID} (A.m ² .kg ⁻¹)	63	65

Table 3. r_1 and r_2 relaxivity values measured at 1.5T, diameter deduced from the NMRD profiles, and saturation magnetization (M_s) deduced from NMRD and SQUID profiles.

Longitudinal r_1 and transverse r_2 relaxivity values, measured at 1.5T and 37°C (Table 4) are good if we compare them to commercial products displaying similar mean hydrodynamic size.²⁹

The saturation magnetization (M_s) determined for NPs10@D2 and D2-2P from NMRD profiles are lower by comparison with SQUID measurements as NMRD profiles allow deducing sample's magnetization as a function of water diffusion around the magnetic core. The grafting rate was determined by correlation between iron to phosphorus amounts in each sample, and by considering that NPs are perfectly spherical (**Table 4**). Iron concentration, as discussed previously, was determined by three different techniques: ICP-OES, AAS and relaxometry. For the quantification of phosphorus, a colorimetric method was performed. Indeed, in the presence of ammonium heptamolybdate, a mineralized sample of dendronized NPs gives an intense blue color due to the formation of a stable complex between free phosphates, originated from the dendrons, and ammonium heptamolybdate (**Eq. 1**).

Equation 1



Obtained results show a small grafting rate difference between the two dendrons, D2 and D2-2P, which can be attributed to the surface covered by the dendrons, since D2-2P shows a bi-phosphonate tweezer occupying a higher surface in comparison to dendron D2 displaying a mono-phosphonate anchor.

The experimental grafting rates were found in agreement with the theoretical ones showing a whole coverage of the NP surface by the dendron.

Table 4. Grafting rates determined by elemental analysis of iron and phosphorus.

	NPs10@D2	NPs10@D2-2P
[Fe ³⁺] (mM)	10.03	10.03
[Dendron] (nbr/L)	1.83.10 ²⁰	1.61.10 ²⁰
[NPs] (nbr/L)	2.85.10 ¹⁷	2.85.10 ¹⁷
Dendron/NP	648±12	573±9
Dendron/nm ²	1.6±0.3	1.85±0.3
Theory Dendron/nm ²	1.4	1.4

All the previous analyses showed good physico-chemical properties of dendronized NPs for biomedical applications. However, a suitable characterization of NPs' organic shell is a real challenge and of utmost importance since OA (here originating from the synthesis method, ie, thermal decomposition) promotes apoptosis and necrosis of healthy cells.³⁰

FTIR spectroscopy gives a qualitative description of grafted molecular species on NPs' surface. Consequently, in order to better identify the coating' chemical structure, ¹H NMR spectroscopy was investigated. Yet, this technique is not suitable for magnetic particles due to the presence of nano-magnets influencing magnetic field heterogeneity and the decrease of ligand mobility bound to the NPs' surface. This effect induces broadening of NMR characteristic peaks, thus complicating spectrum interpretation. To this end, High Resolution Magic Angle Spinning (HR-MAS) was performed on dendronized NPs.

The general principle of HR-MAS is based on recording an NMR spectrum under rotation of the sample at a magic angle (54°74'). The sample rotation at high frequencies minimizes the dipolar interactions responsible for the NMR peaks broadening in conventional NMR.

Fig.6 shows an example of conventional ¹H NMR spectra of OA in CDCl₃ and D2-2P in D₂O compared to NPs10@D2-2P ¹H HR-MAS spectrum in D₂O.

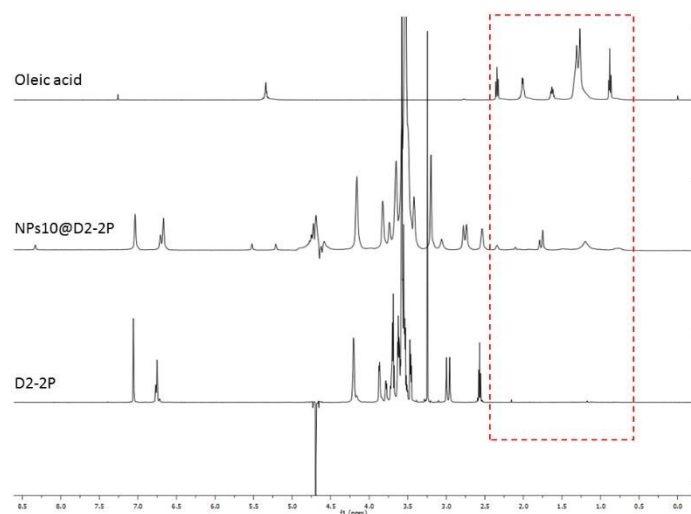


Figure 6. Oleic acid ^1H NMR spectrum in CDCl_3 (top), NPs10@D2-2P ^1H HR-MAS spectrum in D_2O (middle) and D2-2P ^1H NMR spectrum in D_2O (bottom) recorded with a NMR Bruker Avance 500MHz.

The ^1H HR-MAS spectrum shows OA representative peaks at 0.9 - 2.5 ppm corresponding $-\text{CH}_2-$ groups and at 5.2 ppm the signal of vinyl bond $-\text{CH}=\text{CH}-$. D2-2P representative peaks are present between 2.5 and 4.5 ppm, and also at 6.4 and 7 ppm. Moreover, one can notice that OA peaks represented on the ^1H HR-MAS profile are shifted and not all of the peaks can be observed. This phenomenon can be explained by the influence of the solvent nature. Indeed, Polito *et al.* reported that the appearance of NMR signals on a HR-MAS profile, changes as a function of solvent nature due to the modification of ligand mobility.³¹ Dendronized NPs are soluble in D_2O , which is not the case for OA. In deuterated water, OA chains are probably not completely extended since the solvent is much more polar than THF. This could have an effect on the OA molecular mobility, thus reducing the signal intensity and only the signals related to the end of OA chains are visible. These observations confirm thus the presence of OA at the surface of NPs10@D2-2P, leading to the conclusion that the dendron grafting rate is not 100%, as assumed by theoretical calculations.

In vitro studies

Cytotoxicity

Cytotoxicity was assessed through MTT and LDH release assay on 4 different cell lines: i) Human hepatic stem cell line (HepaRG), ii) Hepatocyte derived cellular carcinoma cell line (Huh7-luc), iii) Adenocarcinomic human alveolar basal epithelial cells (A549-luc) and iv) Human neuroblastoma cell line (Kelly). MTT assay were performed after an incubation of 24 or 48 h (ESI, Figure S5) with various concentrations of NPs@D2 and NPs@D2-2P (0.82, 2.05, 5.12, 12.8, 32, 80, 200 and 500 $\mu\text{g/mL}$). Those incubation times were chosen according to *in vivo* studies showing the blood half-life of IONPs varies. It depends on particle size and surface properties,³² from 2 h for Dextran-

coated 120-180 nm Ferumoxide particles (Endorem[®], Feridex[®]) to 24-36 h for Dextran-coated 15-30 nm Ferumoxitran particles (Sinerem[®], Combidex[®]). In a recent study, the half-life of starch-coated or PEG-coated NPs was found to be 0.12, 7.3 (5 kDa PEG) and 11.8 h (2 kDa PEG), respectively, in male rats.³¹ NPs10@D2 demonstrated both an incubation time and concentration dependent cellular toxicity (Fig. 7 top).

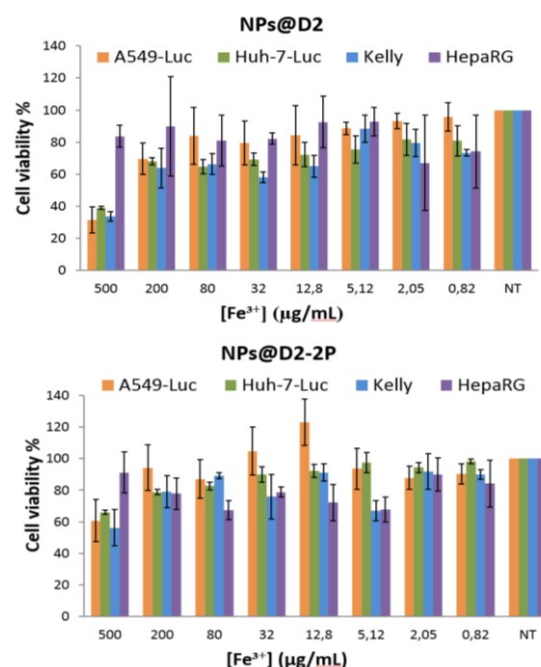


Figure 7. MTT cell viability results obtained with cells transfected with NPs10@D2 (left) or NPs10@D2-2P (right) after 24 h incubation.

After 24 h incubation, NPs10@D2 showed mild cytotoxicity with a cell viability decreasing under 80 % at various concentration depending on the cell line tested, and respectively, 32 $\mu\text{g/mL}$ for A549luc, 5.12 $\mu\text{g/mL}$ for Huh7luc and 12.8 $\mu\text{g/mL}$ for Kelly. At the highest concentration tested (500 $\mu\text{g/mL}$), cell viability drop under 40% for all three cell lines showing a sharp cytotoxicity. After 48 h incubation time the cell survival rate followed almost the same trend with a threshold of cytotoxicity at 32 $\mu\text{g/mL}$ (A549luc), 2.05 $\mu\text{g/mL}$ (Huh7luc) and 5.12 $\mu\text{g/mL}$ (Kelly). It shows that prolonged interaction increase slightly the cytotoxicity. However as 48 h is above the average cell doubling time for all three cell lines tested, the results are not only the reflection of cell mortality but potentially of the influence on cell cycle. On the other hand, human hepatic stem cells HepaRG, showed very low toxicity (at 24 h incubation) and even proliferation effect over time (at 48 h incubation) at the highest applied concentrations (*i.e.*, 500 and 200 $\mu\text{g/mL}$).

NPs10@D2-2P (Fig. 7 bottom) demonstrated a good survival rate after 24 h and 48 h (ESI, Fig. S5) incubation for all cancer cell lines and at Fe^{3+} concentrations up to 200 $\mu\text{g/mL}$. After 48 h incubation, A549-luc cells showed high proliferation rate even at low concentration. At the highest concentration NPs@D2-2P showed an acute cell toxicity with a drop of cell survival rate to 30% for Kelly only.

MTT tests highlighted that IONPs coated with D2 or D2-2P dendrons, modify the cell cytotoxicity. The toxicity of dendronized IONPs may be related to their ability to damage DNA via magnetite oxidation as previously shown by Karlsson *et al.* on cultured cell lines.³³ However our results seem to designate other factors, related to the surface coating and mainly the anchoring group at the Nps' surface, as possibly being responsible for cell toxic responses. The presence of OA on the dendronized NPs' surface could be involved. Indeed, Delgado *et al.* have recently reported OA influence on normal and cancer cell lines.¹⁸ Their results demonstrated that OA alone promotes apoptosis on different cell lines, even though normal cells were expected to be less sensitive towards OA than cancer cells. As shown on the HR-MAS profiles of NPs10@D2-2P (Fig.6), OA is still present at the dendronized NPs' surface. This result assesses the idea of cytotoxicity induced by the existence of OA in the NPs10@Dendron composition.

The cell membrane integrity was determined via quantification of LDH leakage from cells incubated with NPs10@D2 and NPs10@D2-2P (Fig.8).

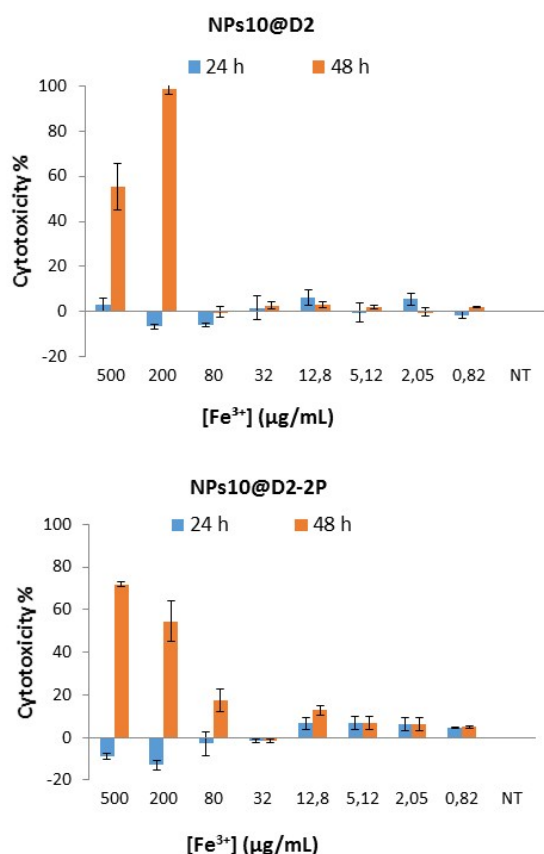


Figure 8. LDH release results obtained for HepaRG cells after 24 and 48h incubation with dendronized nanoparticles.

For the shorter incubation period (24h), HepaRG demonstrated low cytotoxicity (below 10%) for entire range of concentrations and for both dendronized IONPs. Else, at 24h incubation for the highest concentrations (above 80µg/mL), one can notice negative cytotoxicity, which is not a calculation error, on the

contrary, but is due to the formation of iron chelators which assist cell proliferation.

DOI: 10.1039/C7TB00781G

After 48h incubation (ESI, Fig. S5) the trend was completely different as a significant increase (over 60%) in LDH leakage was observed for the highest Fe^{3+} concentrations and above 200µg/mL, both dendronized nanoparticles presenting low cytotoxicity for iron concentrations up to 80µg/mL. Regarding those LDH release tests, it is important to point out that such assay measures the fluorescent signal of membrane-damaged cells, not of the normal ones. Therefore, even though the cell number is increasing as incubation time increases, a natural proliferation process, the LDH leakage assay cannot count the viability of normal cells. It only detects the accumulated LDH derived from continuous leakage of damaged cells which number is proportional to time, as at 48h incubation a programmed cell death occurs, mediated by an intracellular program.³⁴ Furthermore, the real nature of cell membrane morphology changes during contact with nanostructures, which may be accredited to endocytosis as well as possible membrane disruption by potential quantum mechanical effect and other nano-activities.³⁵

Cellular uptake study by flow cytometry

We studied NPs10@Dendron internalization in our different cancer cell lines, as a function of Fe^{3+} concentration, but also as a function of time. Previously reported studies showed that endocytosis is the main mechanism of cellular internalization of magnetic nanoparticles.³⁶ However, internalization is not only due to one distinct pathway but several processes are possible in parallel like passive transmembrane translocation or active internalization process (pinocytosis, clathrin mediated endocytosis etc...). In order to distinguish active from passive mechanism, we studied cellular uptake at various temperatures, *ie* 37°C and 4°C. At 4°C, all active processes are blocked. Indeed cell growth and metabolism are clearly limited at 4°C because of lower membrane fluidity, reduced enzymes' affinity towards their substrates, decreased thermal energy and reaction rates and increased aqueous viscosity.^{37,38}

Cellular uptake was studied by flow cytometry using fluorescently labeled nanoparticles. Dendronized IONPs were decorated with Alexa495-Amine (Dyomics GmbH) via carbodiimide linkage achieved in the presence of N-hydroxysuccinimide in water for 2h. NPs10@D2_Alexa495 and NPs10@D2-2P_Alexa495 were characterized by DLS and Zeta potential (see ESI, Table S1). The Zeta potential shift at pH = 7 showed the successful Alexa dye grafting on the NPs' surface. Furthermore, DLS measurements assessed colloidal stability of Alexa-coupled nanomaterials.

Cells were incubated during 4 and 24h with NPs10@D2_Alexa495 (1 (ESI, Fig. S6) or 10µg of Fe^{3+} /mL) or NPs10@D2-2P_Alexa495 (10 or 50µg of Fe^{3+} /mL (ESI, Fig. S6)). In all FACS analysis, cell debris and free particles were excluded by setting a gate on the plot of side-scattered light (SSC) vs forward-scattered light (FSC).

Acquisition parameters were optimized for detection of Alexa495 fluorophore, excitation at 488nm wavelength with an

argon laser and detection above 505nm. The cellular uptake of dendronized NPs10@D2_Alexa495 and NPs10@D2-2P_Alexa495 by three cancer cell lines (Kelly, Huh7-luc and A549-luc) at varying time periods and temperatures was quantified as percentage of fluorescent cell and results are shown in Fig.9.

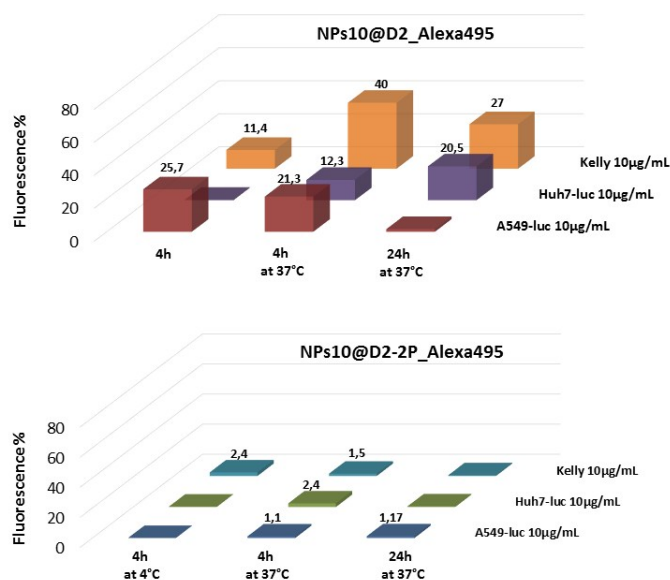


Figure 9. Flow cytometric analysis of A549-luc, Huh7-luc and Kelly cells incubated at different temperatures and times, with a concentration of 10 µg/mL of Alexa495 labeled NPs10@D2 and NPs10@D2-2P.

Internalization of NPs10@D2_Alexa495 at 10 µg/mL (Fig.9) followed the same trend between the three cell lines but with modification in the percentage of fluorescent cell. Altogether, at 37 °C, an internalization process was highlighted at 4h with 21%, 8.73% and 40% of fluorescent cell for respectively A549luc, Huh7luc and Kelly. At 24h fluorescent cells were still detected but their proportion changed from 4h with 5% (A549luc), 20.5% (Huh7luc) and 27% (Kelly). Modification in the percentage of fluorescent cell and so for in the number of cell showing NPs@D2_Alexa495 internalization is the reflect of intracellular processing of NPs after internalization. Indeed exocytosis, an intracellular process leading to the fusion of intracellular vesicle to the plasma membrane and the release of its contents in the extracellular environment, is one of the pathways of endocytosis vesicle. In the incubation time we thus see a snapshot resulting from a balance between endocytic and exocytic processes. It does explain as well the difference between cell lines as it has been proven that endocytic activity is different between cells from different lineage. Interestingly we record cellular internalization at 4°C with 25.7 % (A549luc), 1.2% (Huh7luc) and 11.4 % (Kelly) of fluorescent cell. Passive translocation process seems to take place since at 4°C all active internalization mechanisms are blocked. Moreover experiment performed at 1 µg/mL demonstrate the same profile but with a

clear decrease in percentage of fluorescent cells (from 40% (10 µg/mL to 8.73% (1 µg/mL)) (ESI, Fig S6). It could underscore the non-specific interaction process between NPs@D2 and the cell membrane.

Regarding internalization of NPs10@D2-2P_Alexa495 (Fig. 9): The results of flow cytometry after 4 or 24 h of incubation at 4°C or 37°C revealed no significant uptake of NPs10@D2-2P_Alexa495 whatever the cell lines, the NPs' incubation time or temperature. Taking into account the results of cellular uptake for NPs10@D2_Alexa495 showing highest uptake values for the highest concentration (10µg/mL), it was decided to increase the concentration of NPs10@D2-2P_Alexa495 and use 10 and 50µg/mL for internalization assessment. The same results were recorded at 50 µg/mL (ESI, Fig S6). Such opposite behaviors of D2 and D2-2P dendronized NPs toward cellular uptake could be explained by the presence, at various amounts, of remaining OA at the surface of those nanohybrid structures (Fig.10). Indeed, OA could change the interaction with cell surface and elicit passive membrane translocation by direct interaction of OA with the fatty acids compounds of extracellular membrane. OA is a well-known penetration enhancer that increases membrane permeability.³⁹ Such results mirrored the results of cell cytotoxicity described above.

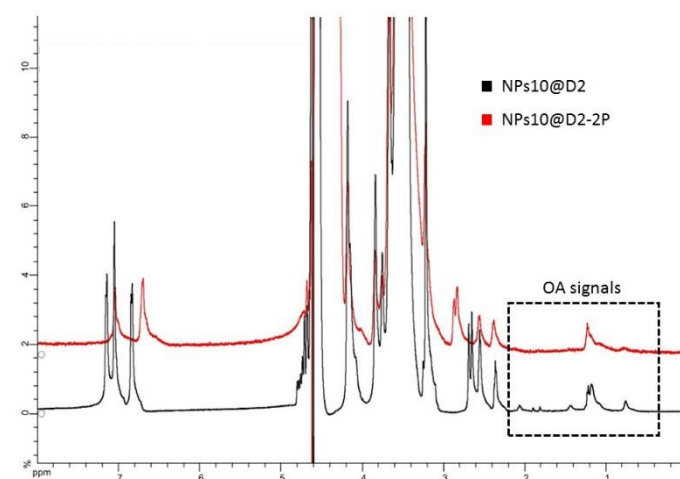


Figure 10. HR-MAS recorded for NPs10@D2 (bottom) and NPs10@D2-2P (top).

Those cytotoxicity assays and cellular uptake tests lean toward the idea that NPs10@D2 presents a higher amount of OA in the final structure in comparison with NPs10@D2-2P. One can explain the highest cytotoxicity and cellular uptake observed for NPs10@D2 showing the highest remaining OA amount at the dendronized NPs' surface.

In vivo MRI studies

The *in vivo* MRI studies were performed on NMRI mice. Fig. 11 shows spin-echo abdomen images of a living mouse acquired before and after intravenous (*iv*) injection of the nanoparticles solution at different times post *iv*.

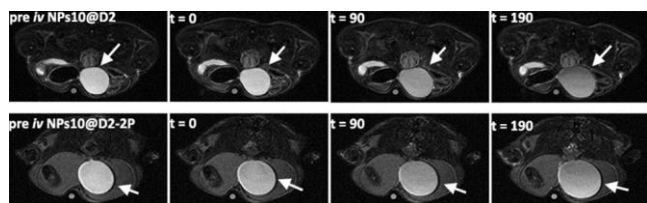


Figure 11. MR images of a live mouse with a T_2 -weighted axial sequence (TR 7726, TE 52). Images were acquired before (pre-contrast) and 0, 90 and 190min after intravenous injection of 70 μ L of NPs10@D2 (top) and NPs10@D2-2P (bottom) at a concentration of 45 μ mol of Fe^{3+} /kg body weight.

A strong negative contrast in the liver in T_2 -weighted images 90min after iv injection (Fig. 11) and an increased negative contrast in urinary bladder T_2 -weighted axial images over 190min post iv (Fig. 12) were highlighted. The negative contrast persisted over 10h in liver and for 6h in bladder, but it weakened over time, suggesting that dendronized nanoparticles are susceptible to renal and hepato-biliary excretions.

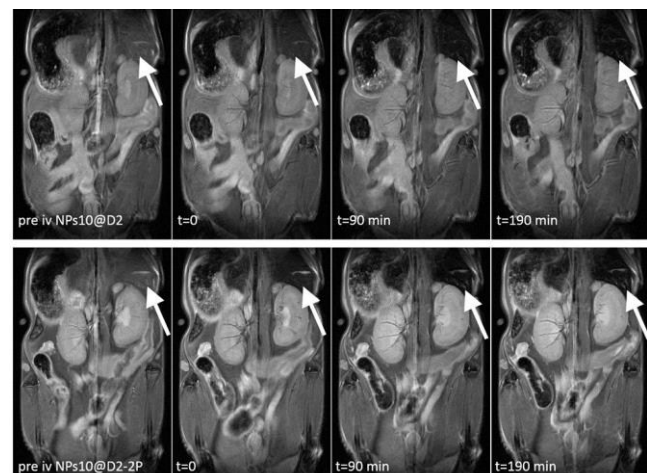


Figure 12. MR images of a live mouse with a T_2 -weighted spin-echo sequence (TR 2000, TE 17). Images were acquired before (pre-contrast) and 0, 90 and 190min after intravenous injection of 70 μ L of NPs10@D2 (top) and NPs10@D2-2P (bottom) at a concentration of 45 μ mol of Fe^{3+} /kg body weight.

The Δ SNR% measured on Rapid Imaging with refocused Echoes (RARE) images of liver and bladder confirmed the negative contrast produced by the dendronized nanoparticles (Fig. 13). The signal intensity in mice injected with NPs10@D2 reached a maximum at 140min post-injection for liver (55%) and 190min post-injection for bladder (33%) (Fig. 13 top). However, mice injected with NPs10@D2-2P showed a maximum of signal intensity (SI) at 45min post-injection for liver and at 140 min post-injection for bladder (Fig. 13 bottom). At 24h post injection of NPs10@D2 or NPs10@D2-2P, the negative contrast for both liver and bladder appeared underneath 20%, showing a clear tendency for nanoparticles' excretion or metabolism. Furthermore, despite the administered dose (triple dose used in clinical trials for humans, 15 μ moles of Fe^{3+} /kg body weight),

all mice showed no toxic signs over 48h, e.g. mice showed regular breathing, good quality walkways, no surrounding tissue irritation.

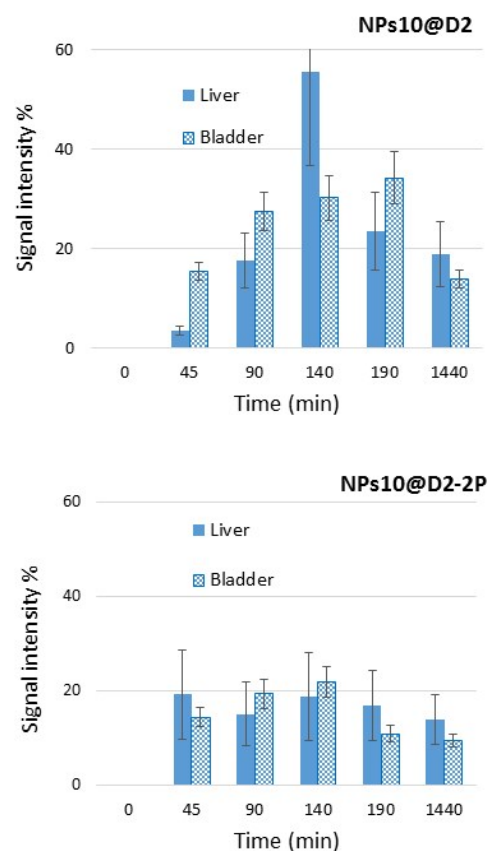


Figure 13. Calculated Δ SNR% for liver and bladder over the time after intravenous injection of NPs10@D2 (left) and NPs10@D2-2P (right).

One must than notice that signal intensity over time recorded in the liver for NPs10@D2 clearly shows a maximum (at 140 min post injection), possibly reflecting metabolism in the liver, whereas the passage is transient for NPs10@D2-2P as it never reaches a maximum. Such result can also be explained by the amount of remaining oleic acid on the surface of the dendronized nanoparticle. Indeed, as we have shown previously (Figure 10), there is a greater amount of oleic acid remaining on the surface of the nanoparticle functionalized with the mono-phosphonic acid dendron (D2) and thus a stronger tendency to be retained in the liver (hydrophobicity), as compared to NPs dendronized through a biphosphonic tweezer (D2-2P).

Materials and Methods

Experimental procedures

The syntheses of organic coatings were performed under an argon atmosphere. The solvents (CH_2Cl_2 , THF, ACN, DMF,

MeOH, EtOH) were distilled or dried over 4 Å molecular sieves. All commercially available reagents were used without further purification. Thin layer chromatography (TLC) analyses were performed on aluminum plates coated with Merck Silica gel 60 F254 and purifications by flash column chromatography were carried out using silica gel 60 and the specified eluent. Nuclear magnetic resonance spectra (^1H and ^{13}C and ^{31}P) were recorded on a 300 MHz spectrometer. Chemical shifts for ^1H ^{13}C spectra are recorded in parts per million and are calibrated to solvent residual peaks (CHCl_3 : ^1H 7.26 ppm; ^{13}C 77.16 ppm; MeOH: ^1H 3.31 ppm; ^{13}C 49.00 ppm; H_2O : ^1H 4.79). Multiplicities are indicated by s (singlet), bs (broad singlet), d (doublet), t (triplet), q (quartet), quin (quintuplet) and m (multiplet). Coupling constants, J , are reported in Hertz. Oligoethylene glycol (OEG) derivatives were purchased from Quanta BioDesign and used without further purification.

Synthesis of 10 nm iron oxides by thermal decomposition

Spherical IONPs were synthesized by the thermal decomposition of iron stearate in octyl ether and led to the *in situ* formation of NPs coated with fatty acids. 1.38 g (2.22 mmol) of $\text{Fe}(\text{stearate})_2$ (Strem Chemicals, 9%Fe, 100g) and 1.24 g (4.44 mmol) of oleic acid (TCI, 99%, 25 mL) were added in 20 mL of dioctyl ether (Sigma-Aldrich, 99%, 100g, b.p. 287°C). The mixture was heated and kept at 110°C under stirring for 60 min in order to dissolve the reactants. The solution was heated up to 330°C for 30 min with a heating rate of 5°C/min without stirring and maintained at 330°C to reflux for 120 min under air. At the end of the synthesis, a viscous black liquid characteristic of NPs formation was obtained. This liquid contains NPs10, undecomposed iron stearate and the excess of OA. NPs10 were then purified and separated from reactants and by-products using a series of precipitation/re-dispersions (washes) in a mixture of good/bad solvents. At first, NPs10 were precipitated by adding acetone (bad solvent 3/4 v/v) to the reaction mixture followed by centrifugation at 10000 rpm for 10 min. Subsequently, the supernatant was removed and the sediment was dispersed in cyclohexane (good solvent 1/4 v/v) to which was added acetone (bad solvent 3/4 v/v) and the mixture was centrifuged at 10000 rpm for 10min. NPs10 purification was FTIR monitored. The as-synthesized NPs, named NP@OA, were then easily suspended in THF.

Functionalization process

5 ml of a NP@OA suspension in THF (1 mg/ml) were put into contact with a suspension of the dendritic phosphonate (D2 or D2-2P) (7 mg). The suspension was magnetically stirred for 48 hours. A ligand exchange occurs leading to a suspension of dendronized NPs. The grafted NPs were then separated from the ungrafted dendrons by ultrafiltration. This technique, well adapted to purify all functionalized NPs water suspensions, involves regenerated cellulose membranes with a nominal molecular weight limit (NMWL) of 30 kDa.

Alexa labeling

20 mg of EDCI were added at 0 °C to a suspension of 5 mg $[\text{Fe}^{3+}]$ NPs10@D2 or NPs10@D2-2P in 5 mL H_2O at pH 6.5. After 30 min of mechanical stirring at 0 °C, 0.25 mg of Alexa495 were added at 0 °C. The suspension was mechanically stirred for 2h at RT. Once the grafting completed, ultrafiltration was performed, monitored by UV-Vis. Size measurement by Dynamic Light Scattering (DLS) and Zeta potential were performed on suspensions at pH 7.4.

Characterization techniques

The NP@OA, before and after grafting, were characterized by transmission electron microscopy (TEM) with a TOPCON 002B microscope operating at 200 kV, (point resolution 0.18 nm) and equipped with a GATAN GIF 200 electron imaging filter. The grafting step was confirmed by infrared spectroscopy using a Fourier Transform Infrared (FTIR) spectrometer (Digilab FTS 3000) (samples were gently ground and diluted in non-absorbent KBr matrices)). The stability of the water suspensions was assessed by measuring the particle size distribution in water by DLS, at pH 7.4 and their zeta potential using a nano-size MALVERN (nano ZS) zetasizer. Hysteresis cycles at room temperature and ZFC/FC measurements between 5 K and 300 K under a field of 75 G, of both as-synthesized and dendronized NPs, were performed with a Superconducting Quantum Interference Device (SQUID) magnetometer (Quantum Design MPMS-XL model). High resolution magic-angle spinning NMR (HR-MAS NMR) experiments were carried out on a Bruker FT-NMR Avance 500 equipped with an 11.75T superconducting ultrashield magnet. All the experiments were performed at spinning rate of 5kHz with a 50µL zirconium rotor. Matrix assisted laser desorption ionization time of flight (MALDI-TOF) mass spectra were acquired using a Bruker spectrometer. High resolution mass spectra were performed on Waters-QTOF spectrometer with electrospray ionization mode.

In vitro studies

Cells

Huh7.luc, human hepatocarcinoma, were kindly provided by Dr Eric Robinet. Huh7.luc stably transfected to express firefly luciferase were propagated in Dulbecco's modified Eagle's medium supplemented with 10% of decomplexed fetal bovine serum, gentamycine (50µg/mL) and non-essential amino acids.

A549luc human lung carcinoma cells (ATCC® CCL-185TM provided by Polyplus transfection®, Illkirch, France), stably transfected to express firefly luciferase were cultivated in DMEM 1 mg.L⁻¹ glucose (EMEM, LGC Stan- dards), 10% FBS, 100 µg.mL⁻¹ penicillin, 100 mg.mL⁻¹ streptomycin (Invitrogen, Carlsbad, CA) and 0.01% geneticin (Geneticin® Selective Antibiotic (G418 Sulfate) (50 mg.mL⁻¹), ref. 10131027, ThermoFisher).

Kelly, human neuroblastoma (ECCAC, ref 92110411) were propagated in RPMI1640 medium supplemented with 10 %

foetal bovine serum, 100 $\mu\text{g.mL}^{-1}$ penicillin, 100 $\mu\text{g.mL}^{-1}$ streptomycin (Invitrogen, Carlsbad, CA).

Cells were plated into 96-wells flat-bottom plates at a starting density of 10^4 cells per well. After an equilibration time (12 to 24h for A549-luc, Huh7-luc and Kelly, and 7 days for HepaRG), until they reached 70%-80% confluency, culture media was removed and cells were treated in triplicate with increasing concentrations (0.82, 2.05, 5.12, 12.8, 32, 80, 200 and 500 $\mu\text{g/mL}$) of NPs10@D2 and NPs10@D2-2P suspended in culture media.

MTT assay

The number of viable cells after NPs10@D2 and NPs10@D2-2P exposure was evaluated by the MTT (3-[4,5-methylthiazol-2-yl]-2,5-diphenyl-tetrazolium bromide) assay. In brief, A549luc cells, Huh7.luc and Kelly (1. 10^4 cells per well) were seeded in a 96-well plate and kept overnight for attachment. HepaRG cell, after cell seeding at 1.104 cell per well in a 96 well plate (Greiner, flat bottom 96 well plate, Dominique Dutscher, ref 20035), were cultivated 7 days to reach 70-80% confluence before testing. The next day the medium was replaced with fresh medium with various concentrations of NPs10@D2 or NPs10@D2-2P diluted in complete culture medium and cells were allowed to grow for 24 h. After completion of incubation, medium was discarded and well thoroughly washed with 200 μL of PBS in order to eliminate all remaining extracellular nanoparticles. 200 μL of cell culture medium + MTT (0.5 mg.mL^{-1}) is added to each well and cells are incubated for further 3h30 at 37°C and 5% CO_2 . After completing the incubation, Medium is carefully discarded and 100 μL of DMSO was added to each well and incubated 15 min at room temperature under orbital shaking. Color developed after the reaction was measured at 550 nm using Xenius microplate reader (SAFAS, Monaco). Cell viability percentage was calculated as the ratio of mean absorbency of triplicate readings of sample wells (A_{sample}) compared to the mean absorbence of control wells (A_{control}). At each experiment DMSO was used as a negative control, A_{DMSO} , as shown in Eq.2:

Equation 2

$$\text{Cell viability \%} = [(A_{\text{sample}} - A_{\text{DMSO}}) / (A_{\text{control}} - A_{\text{DMSO}})] \times 100$$

LDH release assay

LDH release by HepaRG, cultivated in presence of nanoparticles, was assessed using the CytoTox-ONE™ Homogeneous Membrane Integrity Assay (Promega, ref G7890) following manufacturer instructions. Briefly HepaRG cells were seeded in a 96-well plate at a concentration of 1.10^4 cells per well (Microwell Nunc black wall treated for culture cell, Thermofisher ref 165305) and cultivated 7 days to reach 70-80% confluence before testing. Cells were then incubated with 100 μL per well of complete medium with different concentrations of NPs10@D2 and NPs10@D2-2P. After 24 or 48h hours, 100 μL of CytoTox-ONE™ reagent solution was added to each well and incubated for 10min at 25°C in darkness. Subsequently, 50 μL of

stop solution was added to each well, and plates were shaken for 30sec at 25°C. Cells were read under a microplate spectrofluorometer with an excitation wavelength of 560nm and an emission wavelength of 590nm. The cytotoxicity was calculated according to Eq.3, where F_{exp} = measured fluorescence of cells with the testing material; F_{control} = fluorescence of control cells and Max_{LDH} = fluorescence of lysed cells.

Equation 3

$$\% \text{ Cytotoxicity} = [(F_{\text{exp}} - F_{\text{control}}) / (\text{Max}_{\text{LDH}} - F_{\text{control}})] \times 100$$

Flow cytometry

A549luc, Huh7.luc and Kelly (2.10^5 cells per well) were seeded in a 24-well plate (Greiner, Dominique Dutscher, ref 165305) and kept overnight for attachment. Cell were then incubated, with 1 mL per well of NP diluted in complete medium, for 4 or 24h at 37°C in 5% CO_2 . The same experiment has been performed at 4°C for 4h incubation time. Cells were then thoroughly rinsed with 1 mL of cold PBS. Cells were then incubated with 300 μL of trypsin/EDTA solution (GIBCO, Ref R001100, Thermofisher) for 5 minutes. Cells were re-suspended by addition of 500 μL of PBS and harvested by centrifugation at 1000 rpm for 5 min. Cell were re-suspended in 1 mL PBS + 2% paraformaldehyde (PFA) and kept at 4°C protected from light until analysis. Cell fluorescence was analyzed by flow cytometry using a FACScan flow cytometer with Novios software. Cells were analyzed in FL1 canal (Exc 488 nm Em 505 nm). Fluorescence threshold was determined using none treated cells. 10 000 cells were analyzed by sample. Results are reported as the percentage of cell presenting fluorescence above the aforementioned fluorescence threshold.

In vivo studies

All animal experiments were approved by the local animal ethics committee of University of Mons, according to Belgium guidelines regarding the care and use of animals' experimental procedures. The MRI mice ($n = 3$) were anesthetized with isoflurane by inhalation. The experiments were performed on a 400MHz (9.4T) Bruker Biospec imaging system. The contrast agent was injected intravenously at a dose of 45 μmol [Fe^{3+}]/kg body weight. The signal intensity (SI) was measured in regions of interest (ROIs) drawn on the liver and bladder, and in a region situated out of the image of the animal, representing the noise standard deviation (noise SD). The SI enhancement ($\Delta \text{SNR}\%$) was calculated according to Eq.4, where SI_{post} = post-contrast SI, and SI_{pre} = pre-contrast SI.

Equation 4

$$\Delta \text{SNR \%} = \{[(\text{SI}_{\text{post}}/\text{SI}_{\text{noise}}) - (\text{SI}_{\text{pre}}/\text{SI}_{\text{noise}})] / (\text{SI}_{\text{pre}}/\text{SI}_{\text{noise}})\} \times 100$$

Conclusions

Spherical superparamagnetic IONPs were successfully synthesized and grafted with two biocompatible dendrons displaying either one (D2) or two (D2-2P) phosphonic anchors at their focal point. Physico-chemical characterizations assessed their composition, colloidal stability and highlighted suitable magnetic properties as MRI contrast agents. Both dendronized IONPs showed moderate *in vitro* toxicity towards cancer and primary cell lines. Flow cytometry studies performed after 4 or 24 h of incubation at 4°C or 37°C revealed no unspecific uptake of NPs10@D2-2P_Alexa495 whatever the cell lines, the NPs' incubation time or temperature, by opposition with NPs10@D2 which internalized in all cell lines as a function of time and temperature. Such opposite behaviors of D2 and D2-2P dendronized NPs toward cellular uptake could be explained by the presence, at various amounts, of remaining oleic acid (OA) at the surface of those nanohybrid structures. Indeed, OA could change the interaction with cell surface and elicit passive membrane translocation by direct interaction of OA with the fatty acids compounds of the extracellular membrane. Such results mirrored the results of cell cytotoxicity. Furthermore, *in vivo* MRI studies showed high contrast enhancement and renal and hepato-biliary excretions of both dendronized NPs. For all these reasons, IONPs dendronized with the phosphonic tweezer D2-2P and showing no unspecific uptake in cancer cell lines, are clearly a great candidate for early cancer diagnosis imaging and active targeting through post-functionalization with small targeting ligands.

Acknowledgements

The Région Alsace, France, and the University of Mons, Belgium, are gratefully acknowledged for the doctoral fellowship to Catalina Bordeianu. A. Parat, S. Begin-Colin and D. Felder-Flesch thank the Centre National de la Recherche Scientifique (CNRS) for the financial support on A.Parat post-doctoral research position via the DENDRIDIAG project. This research project was also co-funded by the European Regional Development Fund (ERDF) in the framework of the INTERREG V Upper Rhine program, "Transcending borders with every project", project NANOTRANSMED.

This work was also performed with the support of the Fonds National pour la Recherche Scientifique (F.R.S.-FNRS), FEDER, the Walloon Region, the COST Actions, the Centre for Microscopy and Molecular Imaging (CMMI), supported by the European Regional Development Fund of the Walloon Region, and the ARC and UIAP programs.

Notes and references

‡ The manuscript was written through contributions of all authors. All authors have given approval to the final version of the manuscript.

§ Conflict of interest: none.

§§ Abbreviations: ACN, acetonitrile; TMSBr, bromotrimethylsilane; CDCl₃, deuterated chloroform; MeOD, deuterated methanol; D₂O, deuterated water; CH₂Cl₂, dichloromethane; DIPEA, diisopropylethyl amine; DIBALH,

diisobutylaluminium hydride; EDCI, N-(3-Dimethylaminopropyl)-N'-ethylcarbodiimide hydrochloride; EtOAc, ethylacetate; HCl, hydrochloric acid; HOBt, hydroxybenzotriazol; MeOH, methanol; EtOH, ethanol; PAMAM, poly(amido amine); KBr, potassium bromide; NaOH, sodium hydroxide; NaCl, sodium chloride; THF, tetrahydrofuran; r1 and r2, relaxivities; DH, hydrodynamic diameter; RT, room temperature.

- 1 R. M. Kannan, E. Nance, S. Kannan and D. A. Tomalia, *J. Intern. Med.* 2014, **276**(6), 579.
- 2 A. Wei, J. G. Mehtala and A. K. Patri, *J. Control release*, 2012, **164**(2), 236.
- 3 D. A. Tomalia, S. N. Khanna, *Chem. Rev.*, 2016, **116**, 2705.
- 4 A. Rahman, A. K. Rahman, D. A. Tomalia, *Nanoscale Horizons*, 2017, doi: 10.1039/c7nh00010c
- 5 T. Lammers, S. Aime, W. E. Hennink, G. Storm and F. Kiessling, *Acc. Chem. Res.* 2011, **44**(10), 1029.
- 6 M. S. Goldberg, S. S. Hook, A. Z. Wang, J. W. M. Bulte, A. K. Patri, F. M. Uckun, V. L. Cryns, J. Hanes, D. Akin and J. B. Hall, *Nanomedicine* (London), 2013, **8**(2), 299.
- 7 B. Godin, E. Tasciotti, X. Liu, R. E. Serda and M. Ferrari, *Acc. Chem. Res.*, 2011, **44**(10), 979.
- 8 T. D. Schladt, K. Schneider, H. Schild and W. Tremel, *Dalton Trans.* 2011, **40**, 6315.
- 9 A. Walter, G. Cotin, C. Bordeianu, C. Blanco-Andujar, D. Mertz, D. Felder-Flesch and S. Begin-Colin, *Nanomedicine* (Future Medicine) 2016, **11**(14), 1889.
- 10 V. Biju, *Chem. Soc. Rev.* 2014, **43**, 744.
- 11 A. Walter, A. Garofalo, C. Ulhaq, C. Lefèvre, J. Taleb, S. Laurent, L. Vander Elst, R. N. Muller, L. Lartigue, F. Gazeau, C. Billotey, D. Felder-Flesch and S. Begin-Colin, *Chem. Mater.* 2014, **26**(18), 5252.
- 12 J. Shi, X. Yu, L. Wang, Y. Liu, J. Gzo, J. Zhang, R. Ma, R. Liu and Z. Zhang, *Biomaterials*, 2013, **34**, 9666.
- 13 G. Lamanna, A. Garofalo, G. Popa, C. Wilhelm, S. Bégin-Colin, D. Felder-Flesch, F. Gazeau, A. Bianco and C. Ménard-Moyon, *Nanoscale* 2013, **5**, 4412.
- 14 J. Park, K. An, Y. Hwang, J. Park, H. Noh, J. Kim, J. Park, N. Hwang and T. Hyeon, *Nature Materials*, 2004, **3**(12), 891.
- 15 T. J. Daou, J.-M. Grenèche, G. Pourroy, S. Buathong, A. Derory, C. Ulhaq-Bouillet, B. Donnio, D. Guillon and S. Begin-Colin, *Chem. Mater.* 2008, **20**(18), 5869.
- 16 U. Jeong, X. Teng, Y. Wang, H. Yang and Y. Xia, *Adv. Mater.* 2007, **19**(1), 33.
- 17 W. Baaziz, B. Pichon, S. Fleutot, Y. Liu, C. Lefèvre, J.-M. Grenèche, M. Toumi, T. Mhiri and S. Begin-Colin, *Phys. Chem.* 2014, **118**, 3795.
- 18 Y. Delgado, M. Morales-Cruz, C. M. Figueroa, J. Hernandez-Roman, G. Hernandez and K. Griebenow, *FEBS Open Bio*, 2015, **5**, 397.
- 19 T. Marjukka Turunen, A. Urtti, P. Paronen, K. L. Audus and J. H. Rytting, *Pharm. Res.* 1994, **11**(2), 288.
- 20 G. Lamanna, M. Kueny-Stotz, H. Mamlouk-Chaouachi, A. Bertin, B. Basly, C. Ghobril, C. Billotey, I. Miladi, G. Pourroy, S. Begin-Colin and D. Felder-Flesch, *Biomaterials*, 2011, **32**, 8562.
- 21 T. Gillich, C. Acikgo, L. Isa, A. D. Schlu, N. D. Spencer and M. Textor, *ACS Nano*, 2013, **7**(1), 316.
- 22 H. B. Na, G. Palui, J. T. Rosenberg, X. Ji, S. C. Grant and H. Mattoussi, *ACS Nano*, 2012, **6**, 389.
- 23 A. Walter, A. Garofalo, A. Parat, J. Jouhannaud, G. Pourroy, E. Voirin, S. Laurent, P. Bonazza, J. Taleb, C. Billotey, L. Vander Elst, R. N. Muller, S. Begin-Colin and D. Felder-Flesch, *J. Mater. Chem. B*, 2015, **3**(8), 1484.
- 24 K. Kono, *Polym. J.* 2012, **44**, 531.
- 25 W.-M. Liu, Y.-N. Xue, N. Peng, W.-T. He, R.-X. Zhuo and S.-W. Huang, *J. Mater. Chem.* 2011, **21**(35), 13306.

ARTICLE

Journal Name

- 26 B. Basly, G. Popa, S. Fleutot, B. Pichon, A. Garofalo, C. Ghobril, C. Billotey, A. Berniard, P. Bonazza, H. Martinez, P. Perriat, D. Felder-Flesch and S. Begin-Colin, *Dalton Trans.* 2013, **42**, 2146.
- 27 Y. Gossuin, P. Gillis, A. Hocq, Q. L. Vuong and A. Roch, *Nanomedicine and nanobiotechnology*, 2009, **1**, 299.
- 28 S. Boutry, D. Forge, C. Burtea, I. Mahieu, O. Murariu, S. Laurent, L. Vander Elst and R. N. Muller, *Contrast Media Mol. Imaging*, 2009, **4**(6), 299.
- 29 B. Basly, D. Felder-Flesch, P. Perriat, G. Pourroy and S. Begin-Colin, *Contrast Media and Molecular Imaging* 2011, **6**(3), 132.
- 30 M. F. Cury-Bonaventura, C. Pompeia and R. Curi, *Clin. Nutr.* 2004, **23**(4), 721.
- 31 L. Polito, M. Colombo, D. Monti, S. Melato, E. Caneva and D. Prosperi, *J. Am. Chem. Soc.* 2008, **130**(4), 12712.
- 32 C. C. Berry and A. S. G. Curtis, *J. Phys. D. Appl. Phys.* 2003, **36**, R198.
- 33 H. L. Karlsson, P. Cronholm, J. Gustafsson and L. Möller, *Chem. Res. Toxicol.* 2008, **21**(9), 1726.
- 34 D. R. Green, *Cell* 2011, **144**(4), 463.
- 35 A. Kroll, M. H. Pillukat, D. Hahn and J. Schnekenburger, *Eur. J. Pharm. Biopharm.* 2009, **72**(2), 370.
- 36 C. Lu, Y. Hung, J. Hsiao, M. Yao and T. Chung, *Nano Lett.*, 2007, **7**(1), 149.
- 37 C. Gerday, M. Aittaleb, J. L. Arpigny, E. Baise, J. P. Chessa, G. Garsoux, I. Petrescu and G. Feller, *Biochim. Biophys. Acta - Protein Struct. Mol. Enzymol.* 1997, **1342**(2), 119.
- 38 P. Graumann and M. A. Marahiel, *Arch. Microbiol.* 1996, **166**(5), 293.
- 39 S. B. Nielsen, K. Wilhelm, B. Vad, J. Schleucher, L. A. Morozova-Roche, and D. Otzen, *J. Mol. Biol.*, 2010, **398**(2), 351.

View Article Online
DOI: 10.1039/C7TB00781G

